

High-pressure compressibility and thermal expansion of aragonite

SARAH E.M. PALAICH^{1,*}, ROBERT A. HEFFERN¹, MICHAEL HANFLAND², ANDREA LAUSTI³,
ABBY KAVNER¹, CRAIG E. MANNING¹, AND MARCO MERLINI⁴

¹Department of Earth, Planetary and Space Sciences, University of California, Los Angeles, California 90095, U.S.A.

²ESRF, The European Synchrotron, 71, avenue des Martyrs, 38000 Grenoble, France

³Elettra, Sincrotrone Trieste S.C.p.A., S.S. 14 km 163,5 in AREA Science Park, loc. Basovizza, 34149 Trieste, Italy

⁴Dipartimento di Scienze della Terra, Università degli Studi di Milano, Via Botticelli 23, 20133 Milano, Italy

ABSTRACT

The structure and isothermal equation of state of aragonite were determined to 40 GPa using synchrotron single-crystal X-ray techniques. In addition, powder diffraction techniques were used to determine thermal expansion between 298–673 K. At room temperature, aragonite has orthorhombic Pnma structure to 40 GPa, with an isothermal bulk modulus of 66.5(7) GPa and $K' = 5.0(1)$. Between 25–30 GPa the aragonite unit cell begins to distort due to a stiffening of the *c*-axis compressibility, which is controlled by the orientation and distortion of the carbonate groups. The ambient pressure thermal expansion measurements yielded thermal expansion coefficients $\alpha_0 = 4.9(2) \times 10^{-5}$ and $\alpha_1 = 3.7(5) \times 10^{-8}$. The combined results allow the derivation of a thermal equation of state. The new data provide constraints on the behavior of carbonates and carbon cycling in the Earth's crust and mantle.

Keywords: Aragonite, high pressure, thermal expansion, compressibility, equation of state, single crystal, X-ray diffraction

INTRODUCTION

Carbon in the deep Earth consists of a primordial component plus carbonate that has recycled into the Earth's mantle via subduction zones (Dasgupta and Hirschmann 2010; Kelemen and Manning 2015). In the solid state, carbon has limited solubility in mantle silicates and therefore resides chiefly in carbon-rich accessory phases, either as oxidized carbonate or reduced graphite, diamond, or carbide (Shcheka et al. 2006). Aragonite is one of the two most common forms of calcium carbonate found at the Earth's surface and is formed by both biological and physical processes. Although aragonite is metastable at ambient conditions at the surface of the Earth, its biological formation and contribution to ocean floor deposits and high-pressure stability make it the predominant form of calcium carbonate contributing to deep-Earth recycling at subduction zones. Therefore, understanding the phase stability and compressibility of aragonite at high pressures and temperatures will help constrain the behavior of a key potential carbon reservoir in the deep carbon cycle.

At ambient conditions, aragonite has an orthorhombic $2/m$ $2/m$ $2/m$ structure and an average unit-cell volume of 226.93(6) Å³ and a *Z* of 4 (Fig. 1) (Martinez et al. 1996; Santillán and Williams 2004; Ono et al. 2005; Antao and Hassan 2010; Ye et al. 2012). Aragonite becomes stable relative to calcite at ~0.3 GPa (e.g., Johannes and Puhán 1971); however, the pressure of its transformation to a higher pressure (post-aragonite) phase is the subject of debate (Vizgirda and Ahrens 1982; Kraft et al. 1991; Santillán and Williams 2004; Ono et al. 2005; Martinez et al. 1996; Liu et al. 2005). Early shock compression experiments sug-

gested that aragonite undergoes a phase transition around 6 GPa with the possibility of another transition at ~16 GPa (Vizgirda and Ahrens 1982). However, subsequent vibrational spectroscopy experiments found no sign of these phase transitions to 40 GPa (Kraft et al. 1991). X-ray diffraction studies by Santillán and Williams (2004) and Ono et al. (2005) indicated a phase transition near 35–40 GPa but found differing behavior near the transition pressure. Santillán and Williams (2004) noted that strong lattice strain developed between 26 and 40 GPa and suggested that it marked the onset of a sluggish transition to a trigonal structure that became complete at 40 GPa. In contrast, Ono et al. (2005) proposed that the transition was a new orthorhombic structure with *Z* = 2. Studies of high-pressure CaCO₃ by ab initio methods focused chiefly on the transition to post-aragonite and pyroxene-type polymorphs (Oganov et al. 2006, 2008; Arapan et al. 2007; Arapan and Ahuja 2010; Pickard and Needs 2015), but in some cases results identify additional potentially stable structures in the vicinity of the aragonite to post-aragonite transition (e.g., Pickard and Needs 2015).

Insights into the nature and location of the transition to a higher pressure phase can be gained by study of the compressional behavior of aragonite. However, existing X-ray diffraction studies (Martinez et al. 1996; Santillán and Williams 2004; Ono et al. 2005) disagree and lack sufficient detail in the pressure range of the transition.

To address these issues, we conducted a single-crystal synchrotron X-ray diffraction study of aragonite under hydrostatic compression to 40 GPa at ambient temperature in a diamond-anvil cell (DAC). We supplemented compressional results with thermal expansion data from powder X-ray diffraction at ambient pressure. The combination of these studies enables the creation

* E-mail: Palaich@ucla.edu

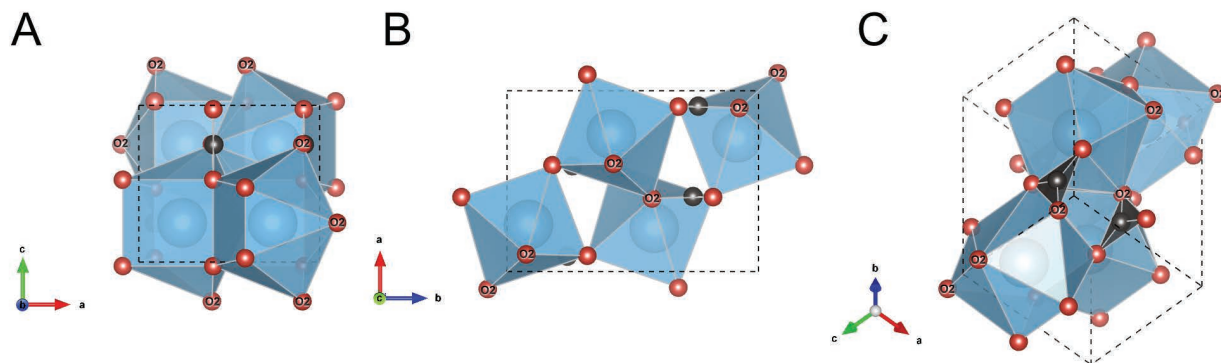


FIGURE 1. Structure of aragonite at ambient pressure and temperature. (a) View along the b -axis; (b) view along the c -axis; (c) slice through the a , b , and c planes. Aragonite is comprised of two planes of triangular carbonate groups in opposite orientation with ninefold-coordinated Ca ions between the carbonate groups. Oxygen atoms are red, Ca atoms and polyhedra are blue, and C atoms and triangles are gray. The O atoms in the O2 position are marked accordingly in each orientation. (Color online.)

of a complete thermoelastic equation of state for aragonite and provides detailed insights into the polyhedral and atomic distortions that accompany compression in the vicinity of the high-pressure breakdown of aragonite.

METHOD

The starting sample of aragonite was a natural specimen from Spain (Molina de Aragon) with a pure composition of CaCO_3 , within experimental accuracy as determined by electron microprobe analysis (University of Milano, Italy). We performed high-pressure single-crystal experiments at the undulator source ID09A beamline at the ESRF, Grenoble, France, following established procedures (Merlini and Hanfland 2013). The optical features of the beamline provide a near-parallel collimated X-ray beam of approximately $15 \times 10 \mu\text{m}^2$ on the sample. The sample was loaded in a Ne pressure-transmitting medium in a membrane-type diamond-anvil cell of Boehler-Almax design equipped with $300 \mu\text{m}$ culet size diamonds and opening windows of 60° . Pressure was determined using ruby fluorescence (Mao et al. 1986). The DAC was mounted on a Omega-rotation goniometer, and single-crystal data were collected by integrated step-scans of 1° , in the 60° rotation range allowed by the geometry of the DAC. The diffraction patterns were recorded with the Mar555 flat panel detector, at a distance of 300 mm from the sample. Aragonite was compressed continuously from ambient pressure to 40 GPa in steps of 1–2 GPa to provide good statistics for equation of state fitting (Table 1). The data were processed with the CrysAlis software (Oxford Diffraction 2008). The instrumental geometrical parameters (sample to detector distance, beam center and detector tilt) were refined with a garnet standard single crystal. The refinement of crystal orientation matrix provided aragonite lattice parameters at variable pressures. The integrated intensity was used for structure refinement, using the software packages Superflip (Palatinus and Chapuis 2007) and Jana2006 (Petricek et al. 2006).

Ambient-pressure thermal expansion measurements were collected on the same natural aragonite sample. Powder diffraction data were collected using a wavelength of 0.689264 \AA at the MCX beamline at the Elettra synchrotron using previously described techniques (Rebuffi et al. 2014). Powdered aragonite was enclosed in a quartz capillary and mixed with quartz as internal standard. A hot glass blower maintained high temperature and measurements were performed in the temperature interval 298–700 K (Table 2). The temperature precision is estimated using the α - β quartz high-temperature transition to be within $\pm 2^\circ\text{C}$. The diffraction patterns were analyzed using the Rietveld method and the GSAS software. The extracted unit-cell volumes were used to fit a simple linear thermal expansion model (Fei 1995; Angel et al. 2014).

RESULTS

Phase stability and lattice compressibility

Single-crystal measurements at ambient pressure and temperature confirm the orthorhombic $Pnma$ space group of aragonite and yield a unit-cell volume of $226.932(5) \text{ \AA}^3$. Figure 2 shows the aragonite lattice compression to 36 GPa at ambient

temperature. The data indicate a decrease in cell volume of $\sim 25\%$ over this pressure range. Below ~ 10 GPa, our results are in good agreement with powder X-ray diffraction studies that used cubic anvil (Martinez et al. 1996) and diamond-anvil cells (Ono et al. 2005; Santillán and Williams 2004). At higher pressures, the new data agree well with those of Martinez et al. (1996) and Ono et al. (2005), but differ from the Santillán and Williams (2004) data. The deviation of the volumes determined by Santil-

TABLE 1. Aragonite unit-cell parameters and volume to 34.8 GPa

P (GPa)	a (Å)	b (Å)	c (Å)	V (Å ³)
0	5.741(4)	7.97(1)	4.959(5)	226.9(2)
0.570(1)	5.712(4)	7.942(2)	4.9491(8)	224.5(2)
1.2(1)	5.690(4)	7.922(2)	4.9433(6)	222.8(2)
2.28(9)	5.651(4)	7.886(2)	4.9276(7)	219.6(2)
2.96(7)	5.627(4)	7.865(2)	4.9192(7)	217.7(2)
3.8(2)	5.602(4)	7.846(3)	4.913(6)	215.9(2)
6.0(1)	5.533(4)	7.789(3)	4.8866(6)	210.6(2)
8.0(2)	5.474(4)	7.743(3)	4.8655(4)	206.2(2)
9.9(2)	5.429(4)	7.711(3)	4.8511(6)	203.1(2)
11.6(2)	5.383(4)	7.675(3)	4.8327(7)	199.6(2)
13.8(3)	5.339(4)	7.651(3)	4.8190(8)	196.9(2)
15.7(6)	5.287(4)	7.616(3)	4.7997(7)	193.2(2)
17.5(5)	5.257(4)	7.598(3)	4.7874(8)	191.2(2)
19.5(3)	5.216(4)	7.580(3)	4.7749(8)	188.8(2)
21.1(4)	5.184(4)	7.558(3)	4.7583(8)	186.4(2)
22.8(2)	5.153(4)	7.542(3)	4.7487(8)	184.5(2)
24.03(2)	5.130(4)	7.538(3)	4.7408(8)	183.3(2)
25.38(7)	5.117(4)	7.527(3)	4.7367(8)	182.4(2)
26.7(1)	5.09(4)	7.514(3)	4.7270(8)	180.9(2)
27.9(1)	5.076(4)	7.504(3)	4.7168(8)	179.6(2)
29.1(2)	5.058(4)	7.490(3)	4.7130(8)	178.5(2)
31.4(2)	5.026(4)	7.475(4)	4.6980(8)	176.5(2)
32.9(2)	4.986(2)	7.502(4)	4.687(4)	175.3(2)
34.8(3)	4.948(2)	7.507(4)	4.663(4)	173.2(2)

TABLE 2. Aragonite unit-cell parameters and volume from 298 to 673 K

T (K)	a (Å)	b (Å)	c (Å)	V (Å ³)
298	5.7457(2)	4.9638(2)	7.9728(3)	227.39(2)
303	5.7462(2)	4.9634(2)	7.9722(3)	227.37(2)
323	5.7501(2)	4.9644(2)	7.9748(3)	227.65(2)
348	5.7553(2)	4.9655(2)	7.9789(3)	228.02(2)
373	5.7603(2)	4.9671(2)	7.982(3)	228.38(2)
398	5.7661(2)	4.9676(2)	7.9858(3)	228.75(2)
423	5.7716(2)	4.9687(2)	7.9899(3)	229.13(2)
473	5.7822(2)	4.9711(2)	7.9961(3)	229.84(2)
523	5.7931(2)	4.9734(2)	8.0054(3)	230.65(2)
573	5.8035(2)	4.9754(2)	8.0151(3)	231.44(2)
623	5.8149(2)	4.978(2)	8.024(3)	232.27(2)
673	5.8279(2)	4.9794(2)	8.033(3)	233.11(2)

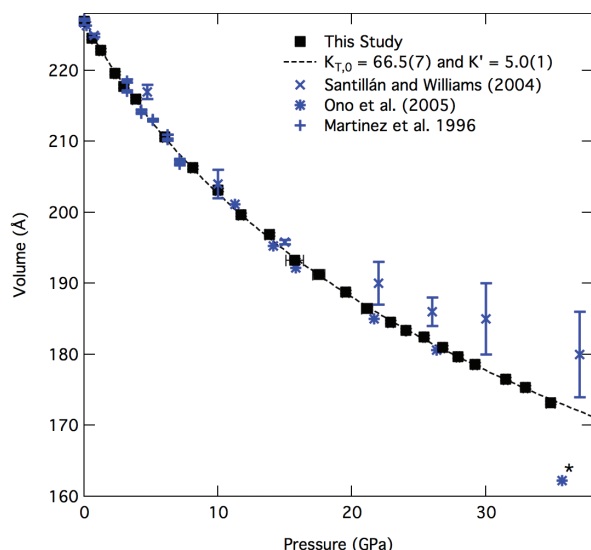


FIGURE 2. Aragonite unit-cell volume vs. pressure. Volume vs. pressure data from this study and three previous investigations of aragonite. The dashed black line represents the fit of the data to the third-order Birch-Murnaghan equation of state. The starred point in Ono et al.'s (2005) data are a post-aragonite structure found after heating by the authors at 35 GPa. (Color online.)

lán and Williams above 10 GPa likely resulted from freezing of the methanol-ethanol mixture they used as a pressure medium, resulting in non-hydrostaticity in their diamond-cell experiments. Ono et al. (2005) addressed this problem by laser heating their aragonite sample in a DAC to reduce differential pressure effects in the sample chamber and to overcome kinetic inhibition of any phase transitions. Data were collected at ambient temperature after cooling. Their data agree with our results to 27 GPa. The next pressure at which Ono et al. (2005) obtained data was 35 GPa, where they identified a large decrease in volume, which they interpret to be due to transformation to post-aragonite structure.

The data were fitted to a third-order Birch-Murnaghan equation of state using a linear least-squares fitting method with V_0 fixed at $226.932(5) \text{ \AA}^3$, the ambient-pressure measurement. Data at >31.5 GPa begin to depart from the Birch-Murnaghan functional form, perhaps due to lattice distortion signaling the onset of the phase transition. To ensure exclusion of data compromised by lattice distortion, only results from ≤ 31.5 GPa were used to derive the isothermal equation of state. This yields an isothermal bulk modulus of aragonite of $66.5(7)$ GPa with $K' = 5.0(1)$. The values agree well with previous values from X-ray diffraction (Martinez et al. 1996; Ono et al. 2005) and Brillouin scattering (Liu et al. 2005) experiments, in which derived bulk moduli were, respectively, 64.8, 73(2), and 68.9(14) GPa ($K' = 4$). Ono et al. also fitted K' , obtaining a bulk modulus of $67(6)$ GPa and $K' = 4.7(8)$, again in excellent agreement with our result.

The compressibility of the lattice parameters of aragonite provides insight into the lattice-dependent elasticity, the mechanism of compressibility, and the onset of phase transformations. The pressure evolution of the normalized values of the a , b , and c lattice parameters of aragonite is shown in Figure 3. The lattice compressibilities were determined by fitting a third-order

Birch-Murnaghan equation to the cubed lattice parameters as a function of pressure. The a -axis is most compressible, with a bulk modulus of $46.0(5)$ GPa and $K' = 2.93(5)$. The c -axis is the least compressible with $K = 122(2)$ GPa and $K' = 5.6(3)$. The b -axis displays a change in compressibility at ~ 15 GPa. Below this pressure, the fit to the data yields a bulk modulus of $59(2)$ GPa with $K' = 11.4(7)$. In contrast, at >15 GPa the pressure dependence flattens, indicating a stiffening of the b -axis. Although the relative compressibilities of each lattice parameter follow trends similar to those determined by Santillán and Williams (2004) and Martinez et al. (1996), our values disagree in detail. Martinez et al. (1996) found both the b and c axes to be more compressible to their highest pressure of 7 GPa. The small pressure range of their experiment limits the accuracy of their results when applied to higher pressure data such as our own. We interpret the difference between our measured compressibilities and the apparent lower compressibility inferred from the Santillán and Williams (2004) data as arising from non-hydrostatic pressure in their sample chamber above 10 GPa.

Axial ratios and polyhedral evolution

Figure 4 shows the c/a , b/a , and b/c axial ratios as a function of pressure. These plots demonstrate significant mechanical distortion of the aragonite unit-cell volume with compression. The c/a and b/a ratios increase continuously as pressure rises. The c/a and b/c ratios of Martinez et al. (1996) agree reasonably well with our data to 7 GPa, the highest pressure in their study. Our results also agree with those of Santillán and Williams (2004) below 10 GPa; however, their data become scattered at higher pressures where their cell lost hydrostaticity. The new, more densely spaced measurements reveal that the change in c/a ratio on compression is slightly nonlinear (Fig. 4a). The

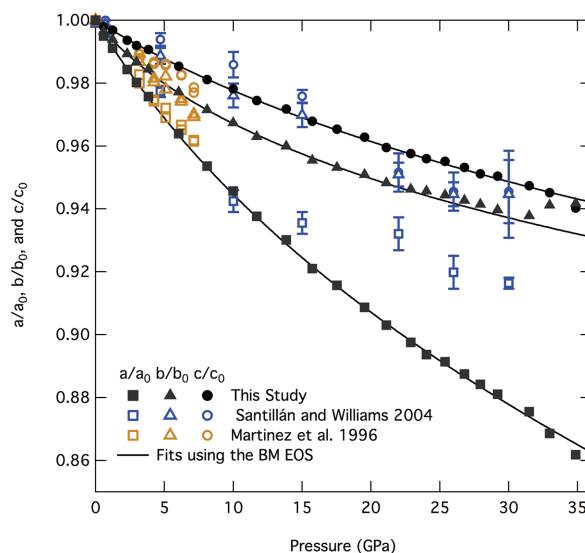


FIGURE 3. Compressibility of a , b , and c crystallographic axes of aragonite. The a -axis is the most compressible and the c -axis is the least compressible. The b -axis changes its compression behavior and begins to stiffen ~ 20 GPa. The data from Santillán and Williams (2004) is consistent to 10 GPa, which is the pressure at which their methanol:ethanol pressure medium freezes and becomes non-hydrostatic. (Color online.)

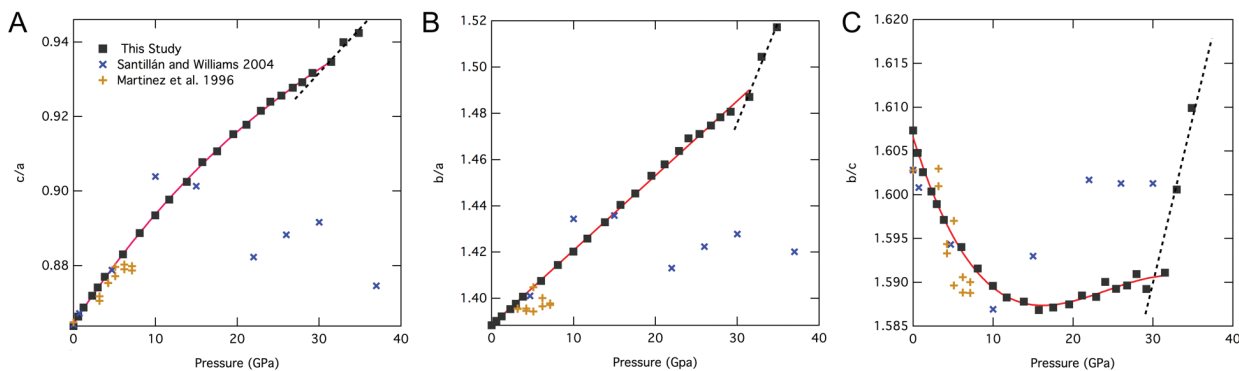


FIGURE 4. Ratios of aragonite: (a) c/b , (b) b/a , and (c) b/c . Data from two previous studies are included in all three figures. The c/b ratio in a maintains a constant trend (red line) until 30 GPa and then changes to steeper slope (dashed line). The b/a ratio is linear throughout. The ratio with constant slope to ~ 30 GPa (red line) before dramatically shifting to a steeper grade (dashed line). The b/c ratios declines steadily to 15 GPa and begins to bottom out, remaining nearly constant to 30 GPa (red line) where it shoots up in a linear trend (dashed line). Each of these changes are consistent with the stiffening of the b -axis relative to the a and c axes. (Color online.)

curvature indicates that the a -axis increases in compressibility relative to the c -axis, which is the least compressible axis (Fig. 3). The change in the ratio above 31.5 GPa (dashed black line in Fig. 4a) indicates a large increase in the compressibility of the a -axis relative to the c -axis. The b/a ratio is linear throughout its pressure range. A dramatic shift occurs at ~ 30 GPa where the b -axis becomes significantly less compressible than the a -axis (Fig. 4b). The large change in slope arises from commensurate increase in a -axis compressibility and decrease in b -axis compressibility above 30 GPa.

The b/c ratio (Fig. 4c) decreases to a minimum at ~ 15 GPa and then increases slightly to ~ 30 GPa. The b/c ratio rises dramatically above this pressure. This behavior is confirmed (as well as the patterns in Figs. 4a and 4b) by an additional data set taken at high pressure and included in this study as Supplemental Material¹. Data from Martínez et al. (1996) and Santillán and Williams (2004) show a similar trend to ~ 10 GPa, as with c/a and b/a , the data of Santillán and Williams (2004) deviate at higher pressure. As with the b/a ratio, the change in slope in b/c at ~ 30 GPa is an indication of severe stiffening of the b -axis (Fig. 3). Santillán and Williams (2004) noted that when the b/c ratio reaches 1.73, the orthorhombic symmetry degenerates to trigonal symmetry. Santillán and Williams (2004) found this to occur at 40 GPa and our data support evolution toward this value due to the stiffening of the b -axis. Subsequent work by Ono et al. (2005, 2007) indicate that the post-aragonite phase is orthorhombic and that the transition pressure is lower than that expected for the breakdown to trigonal symmetry. We are likely seeing evidence for structural distortions at or near conditions of aragonite breakdown as the axial ratios diverge abruptly from their previous trends.

The compressibility of the axes is directly related to the orientation and compressibility of the constituent polyhedra. The plane created by the b and c axes is parallel to the carbonate groups in

the aragonite structure, whereas the a -axis is perpendicular to them (Fig. 5). The high compressibility of the a -axis results from the orientation the relatively rigid carbonate groups, which give no support to compression along the a -axis (Ross and Reader 1992). Accordingly, compression is accommodated by geometric changes in the Ca-O polyhedra. The average compression of the Ca-O polyhedra below 31.5 GPa, as fit to the third-order Birch-Murnaghan equation of state, gives a bulk modulus of 62(2) GPa with $K' = 7.1(5)$. This is within error of the compressibility of the b -axis below 15 GPa and is likely the initial driving force of its compression.

Unlike the Ca-O polyhedra, the carbonate groups are relatively incompressible at these pressures (though they do exhibit small but significant distortions; see below). At ambient pressure and temperature, the distance between triangular carbonate groups is 2.881(13) Å along the a -axis, 4.949(5) Å along the c -axis and 7.942(15) Å along the b -axis. The change in these separations with pressure is a good indicator of the compressibilities of the axes with which they are aligned. Figure 5 compares the aragonite unit cell at ambient pressure and at 32.9 GPa. The carbon and O2 atoms lie along the b -axis and the base of the carbonate triangle lies along the c -axis. A decrease in the end-to-end separation of the relatively rigid carbonate triangles and the alignment of the triangle base with the c -axis account for its lower compressibility. The increasing compressibility of the a -axis is due in part to the small tilting of the carbonate groups, identifiable by the O2 atoms dipping out of the b - c plane toward the a -axis.

Figure 6 compares the ratio of the distances between the carbonate groups along the c and b axes to the b/c ratio (Fig. 4c). The nearly identical dependence on pressure suggests that the intercarbonate distances control the changes in b/c axial ratio. Study of the carbonate-carbonate distances identifies two dips in b/c at ≥ 30 GPa. These dips may be caused by the effects of the distortion of the carbonate groups on the lattice parameters and intracellular dynamics (discussed further in the next section). Measurements of the carbonate separation distance indicate that the b -axis becomes less compressible starting at ~ 15 GPa and that it becomes stiffer than the c -axis between 25–30 GPa.

¹Deposit item AM-16-75528, Supplemental Material and CIF. Deposit items are free to all readers and found on the MSA web site, via the specific issue's Table of Contents (go to <http://www.minsocam.org/MSA/AmMin/TOC/>).

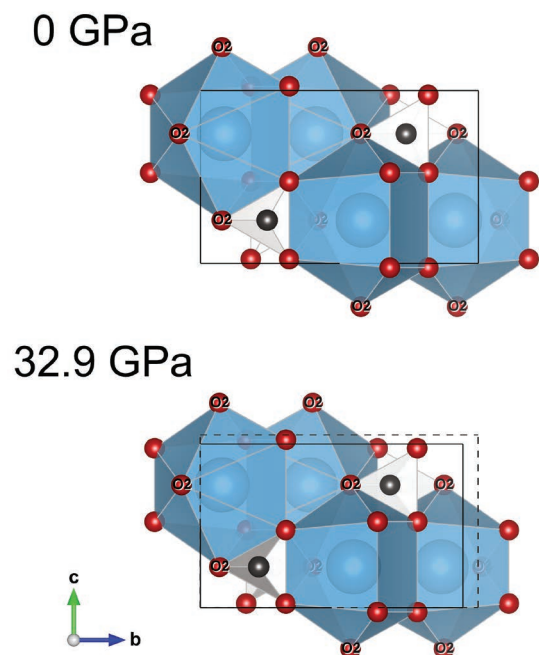


FIGURE 5. Unit-cell comparison at ambient and 32.9 GPa. Shows slice through the a -axis, with the c -axis in the vertical and b -axis in the horizontal. Oxygen atoms are red, carbon are black and Ca are light blue. The carbonate groups are white. The ambient pressure unit cell is overlaid (dashed rectangle) over the unit cell at 32.9 GPa to emphasize the changes in both the b and c axes. (Color online.)

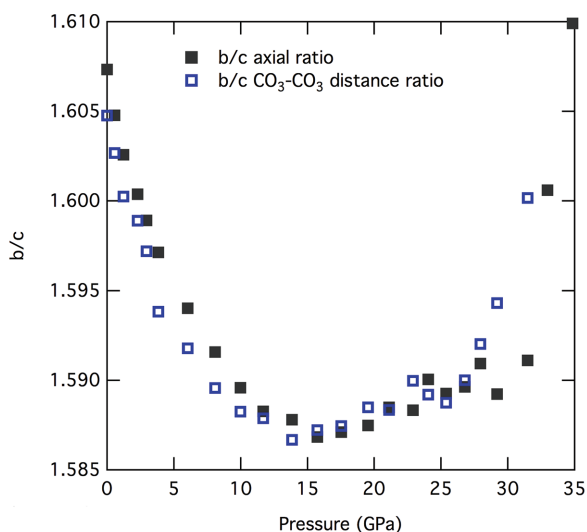


FIGURE 6. Ratio of b/c from unit-cell parameters and $\text{CO}_3\text{-CO}_3$ distances. The solid black squares are the same as those found in Figure 4c. The open blue squares give the ratio of the distance between carbonate groups along the b -axis and carbonate groups along the c -axis (best visualized in Fig. 5). The ratio of the inter-carbonate distances is nearly identical to that of the unit-cell parameters and follows the decreasing trend followed by a change in slope at 30 GPa, which is consistent with the distance between carbonate groups along the b -axis ceasing to decrease after ~ 20 GPa due to the elongation of the carbonate triangles along the b -axis. (Color online.)

This is consistent with an upcoming phase transition between 30 and 40 GPa, as found experimentally by Santillán and Williams (2004) and Ono et al. (2005), and predicted by ab initio studies (Oganov et al. 2006; Arapan and Ahuja 2010; Pickard and Needs 2015). The post-aragonite structure found by Ono et al. (2005) has a lower Z (2, not 4) and its b -axis is $\sim 40\%$ shorter with respect to the a - and c -axes than that found in the ambient orthorhombic aragonite structure. This reduction in the relative b -axis length is smaller than the 50% decrease in formula unit (Z) and indicates that the b -axis remains stiff in the new structure. Experimental work on the lattice geometry of post-aragonite is needed to confirm this conclusion.

Atomic evolution and polyhedral distortion

The evolution with pressure of the atomic positions in the unit cell is shown in Figure 7. The carbon atoms at the center of the carbonate groups move with the O1 atomic position in both a and c axial directions. With compression, the carbon and O1 positions show little movement and no correlation along the b -axis, which is consistent with their nearly perpendicular alignment in this direction (Fig. 5). The Ca atomic position moves linearly in each axial direction and undergoes only a minor shift in position, consistent with the oxygen atoms compressing

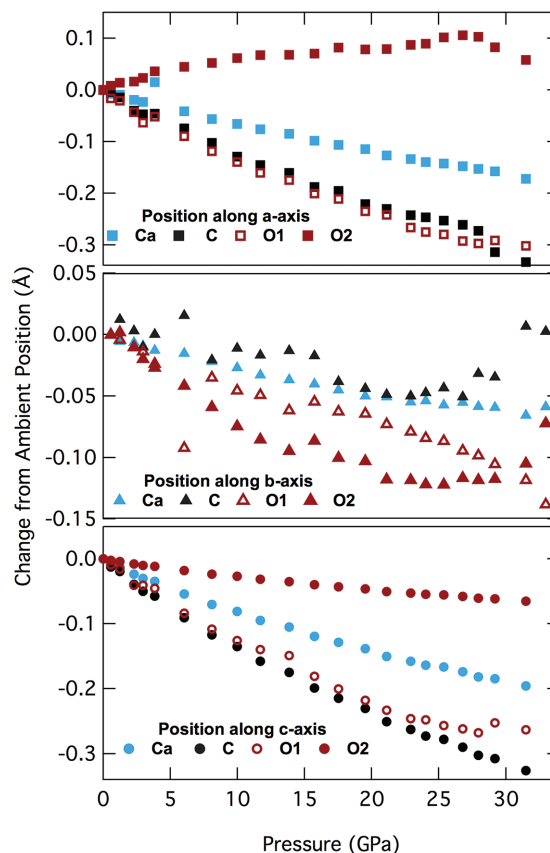


FIGURE 7. Pressure-dependent atomic positions. From the single-crystal refinement data the evolution of the atomic sites is plotted as a function of pressure in the a , b , and c orientations. Positions are plotted as distance from original position in angstroms, normalized for contracting unit-cell volume. (Color online.)

around a relatively stationary Ca atom. The O2 atomic position remains fairly constant in its position along the *c*-axis, but undergoes notable changes in the other two atomic planes. This observation is consistent with large compressional displacement along the *a*-axis as the stacked carbonate groups move closer together and tilt and with the changing compressibility of the *c*-axis. Along the *a*-axis, the O2 position increases with respect to its original position to ~25 GPa, and then dips back toward its original coordinate at 25–30 GPa, the same pressure range as the dip in CO₃-CO₃ distance along the *b*-axis (Fig. 6). Similar behavior is seen in the *b*-axis where the O2 position initially has a negative linear trend compared to its initial position that becomes a reversal near 25 GPa, much like the behavior seen in the *b/c* axial ratio in Figure 4c and the evolution of the carbonate spacing ratio in Figure 6. These shifts bring the O2 position out of initial alignment with both carbon and calcium atoms as can be seen in the *b-c* plane slices at 0 and 32.0 GPa in Figure 5. Figure 5 shows that the central carbon atom in both carbonate groups displaces to left during pressure increase, creating a distortion of the CO₃ triangles in the *b-c* plane. In addition, the O2 atoms dip into *a*-axis as the carbonate planar groups tilt slightly into the *b-c* plane with the O2 arrow side tilting down.

The carbonate groups undergo small but important changes in geometry. Figure 8 gives the evolution of the bonds (Fig. 8a) and angles (Fig. 8b) within the carbonate structure. Both the C-O1 and C-O2 bond lengths remain within close range of their ambient values ≤20 GPa. Above this pressure the bond lengths between the C-O1 and C-O2 diverge. The C-O2 bond continuously shortens between 20 and 29.1 GPa where C-O bond length measurements became unreliable due to lattice distortion. The C-O1 bond length increases over the same pressure range, although at a less dramatic rate. The bond angles reflect the changing geometry demonstrated in the bond lengths. At ambient pressure, the carbonate groups

define equilateral triangles, with both bond angles equal to 120°. Distortion begins almost immediately and the bond angles do not return to 120° as compression continues. The O1-C-O1 bond angle decreases while the two O1-C-O2 bond angles increase before relaxing slightly near ~20 GPa. This divergence occurs before any noticeable changes in bond length arise in the same pressure range (Fig. 8a). Above ~20 GPa, the two O1-C-O2 bond angles continually diverge from the O1-C-O1 angle and the two types end with a 10° difference in angle at 29.1 GPa.

These changes in the carbonate groups are visualized in the overlaid carbonate triangles in Figure 9. The groups clearly evolve from an equilateral to an isosceles triangle at high pressure. The tilt of the O2 atoms in the *a*-axis is apparent in Figures 9b and 9c, which also shows a small deflection of the O1-C-O1 stacking from linear. The stages of change in the carbonate groups are in alignment with the changes observed in the *b/c* ratio. The decrease in bond length and divergence in angle are concurrent with the reversal in the *b/c* ratios in Figures 4c and 6. The increase in slope and significant reduction in the compressibility of the *b*-axis correlate directly with the divergence in both bond length and angle and the shift from equilateral to isosceles. Compression along the *b*-axis begins to stiffen as soon as the carbonate groups begin to distort affecting the overall lattice and leading the rebound in the *b/c* ratio. Effects on other lattice parameters are not apparent until near ~30 GPa when all the ratios under and abrupt change in slope (Fig. 4).

The distance from the O2 atoms to the base of the triangular carbonate group decreases by 1.9% to 31.5 GPa while the *b*-axis itself compresses 6.2%. This difference is another illustration of how the distortion of the carbonate group contributes to increasing stiffness along the *b*-axis with pressure. The *c*-axis compresses evenly despite the bond angle between O1-C-O1 decreasing by 9° over the entire pressure range. The carbonate

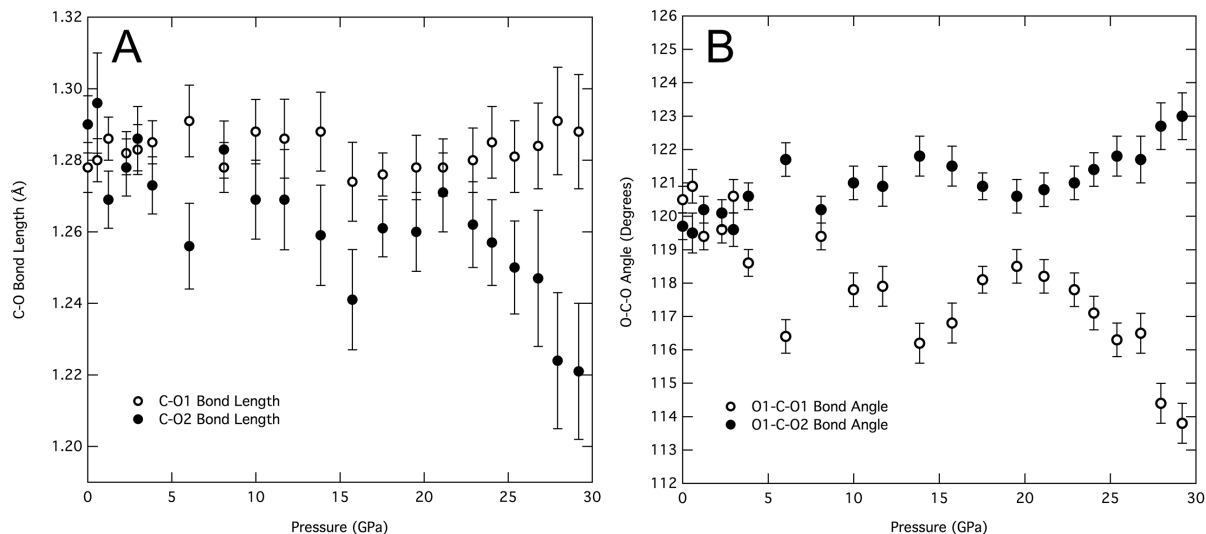


FIGURE 8. (a) C-O bond lengths and (b) O-C-O bond angles. The carbon and oxygen bond lengths are shown for both the O1 and O2 sites. The O1 sites are parallel to the *c*-axis, comprise the base of the carbonate triangle and change very little with pressure. The O2 site bisects the base of the triangle and is in alignment with the *b*-axis. At ~20 GPa, the C-O2 bond distance rapidly decreases and in turn leads to the U-shaped behavior in the *b/c* ratio and eventual lattice distortion between 25–30 GPa. The bond angles steadily diverge from ~20 GPa onward, in alignment with the U-shape in Figures 4c and 6.

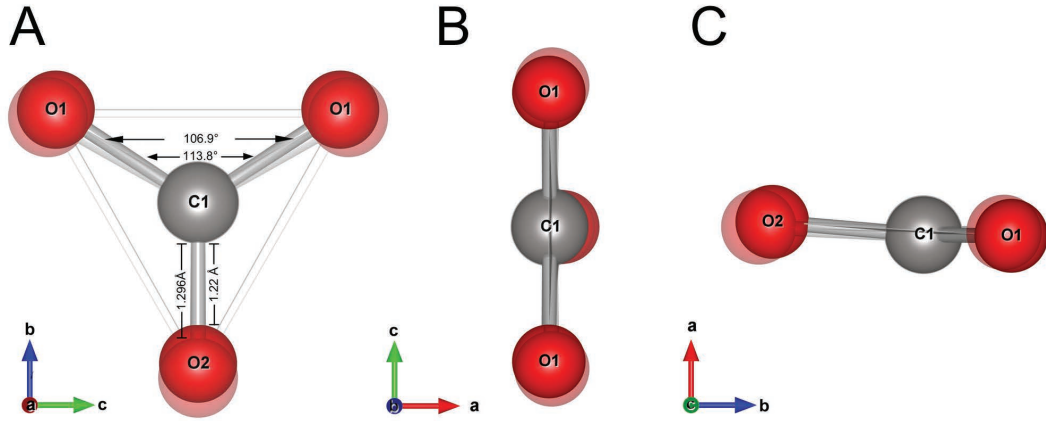


FIGURE 9. Evolution of the carbonate groups in the aragonite structure overlaid at two pressures from three angles: (a) *b-c* planar view with significant changes in bond lengths and angles, (b) *a-c* planar view where the displacement of the O2 oxygen is noticeable, and (c) *a-b* planar view illustrating the change in angle between O1-C-O2. The carbonate groups with all atoms gray are extracted from data at 0 GPa. Carbonate groups with oxygen atoms in red are extracted from data at 29.1 GPa. Carbonate is shown in gray in the center and oxygen is either gray or red depending on pressure. O1 and O2 oxygen sites are labeled. (Color online.)

group O1-O1 distance decreases by 5.6% to 32.9 GPa, essentially the same as the *c*-axis at 5.2% compression over the same range. Thus, the compressional behavior of aragonite can be seen to be a consequence of small, but significant, changes in the most rigid polyhedral elements, the carbonate groups.

Thermal expansion

Figure 10 shows the ambient-pressure thermal expansion data gathered during the powder X-ray diffraction experiment. The measurements are in good agreement with previous data from both Antao and Hassan (2010) and Ye et al. (2012). The thermal expansion of aragonite was fitted using the formalism:

$$V(T) = V_0 \exp \left\{ \int_{T_{\text{ref}}}^T \alpha_V(T) dT \right\} \quad (1)$$

$$\alpha_V(T) = a_0 + a_1(T) \quad (2)$$

where $\alpha_V(T)$ is thermal expansion, a_0 and a_1 are fitted constants, V_0 is the ambient-temperature volume, T is the temperature and T_{ref} is a reference temperature, usually 300 K. The fit of the new thermal expansion data provide the following coefficients: $a_0 = 4.9(2) \times 10^{-5}$ and $a_1 = 3.7(5) \times 10^{-8}$. These results are in agreement with recent measurements by Ye et al. 2012 yielding $a_0 = 4.6(2) \times 10^{-5}$ and $a_1 = 5.4(4) \times 10^{-8}$ (143–586 K), but conflict with other literature data (Antao and Hassan 2010; Martinez et al. 1996). Antao and Hassan (2010) found $a_0 = 5.47(4) \times 10^{-5}$ and $a_1 = 6.1(2) \times 10^{-8}$ (300–750 K), which is 11% greater in a_0 and 64% larger in a_1 . Figure 10 indicates that the data from Antao and Hassan (2010) are in exceptional agreement with the new measurements, which implies that the discrepancy must be in the fitting process. All the experiments indicate that the *a*-axis exhibits the greatest thermal expansion and the *c*-axis the least. The thermal results correlate well with the compressibility study. The *a*-axis is the most compressible and the most expandable. The *c*-axis is the least compressible and the least expandable.

IMPLICATIONS

This study has generated a new isothermal equation of state for aragonite up to 40 GPa, where aragonite likely undergoes a phase transformation. Our new equation of state agrees with previous hydrostatic data (Ono et al. 2005; Liu et al. 2005) and our observation of structural changes at high pressures agrees with previous observations (Martinez et al. 1996; Santillán and Williams 2004; Ono et al. 2005), but the equation benefits from higher sampling density and improved precision in the present study. Our measurements also permit quantification of

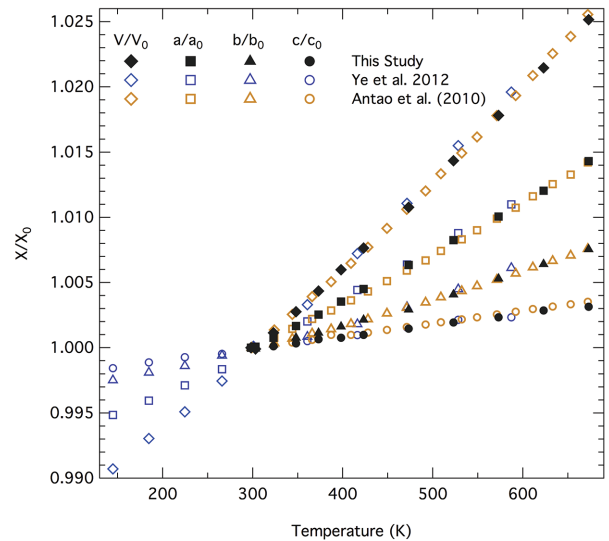


FIGURE 10. Thermal expansion of aragonite unit-cell volume and axial crystallographic parameters. Thermal expansion data from our study is shown in solid black. Data from Ye et al. (2012) and Antao and Hassan (2010) is provided for comparison. We find the *c*-axis to exhibit the most expansion and the *a*-axis to be the least expansive. This is in direct contrast to the compressional behavior where *a* is the most compressible and *c* is the least. (Color online.)

the evolution with pressure of the aragonite axial parameters and the internal behavior of the polyhedral constituents of the unit cell. Significantly, we have identified a reduction in the compressibility of the *b*-axis, which is directly linked to distortions of the carbonate groups and their change from equilateral to isosceles. The distortion of the carbonate groups through the divergence of the C-O1 and C-O2 bond lengths is especially intriguing. Future study of such internal displacements in the carbonate group may give insight into its transformation into a fourfold-coordinated tetrahedral as predicted by Oganov et al. (2006), Arapan et al. (2007), and Arapan and Ahuja (2010) and experimentally observed in aragonite by Ono et al. (2007), in Fe-rich carbonates by Boulard et al. (2012), in ferromagnesite by Boulard et al. (2015) and in Mg₂Fe₂C₄O₁₃ by Merlini et al. (2015).

These results also provide insight into the distortion of the aragonite structure before the phase transition, which is both predicted (Oganov et al. 2006; Arapan and Ahuja 2010; Pickard and Needs 2015) and observed between 30–40 GPa (Santillán and Williams 2004; Ono et al. 2005). Using *ab initio* calculations, Pickard and Needs (2015) predict a monoclinic *P*2₁/*c* structure to be most stable between 32–48 GPa, which correlates directly with our abrupt change in axial ratios and the appearance of large lattice distortion above 29.1 GPa. Our data validate a transition in the range, but give no further insight in the exact structure adopted by aragonite at these pressures. Indeed, this new structure does not exactly fit previous experimental data of post aragonite found by Ono et al. (2005), but there may be kinetic effects hindering the transition or discrepancies caused by the laser heating techniques used in the experimental study. Nevertheless, the aragonite data in this study provides significant insight into the behavior of aragonite and its constituent polyhedra as these transition pressures approach. Kinetic effects may explain why our data maintain the distorted aragonite structure to the highest pressure from which we could extract good data (34.8 GPa) instead of undergoing a transition. The diverging axial ratios and distortion of the lattice indicate that a transition may be taking place sooner than the 40 GPa pressure reported in previous studies.

Our thermal expansion data bolsters the database of aragonite's thermal expansion measurements and confirms the findings of previous studies (Ye et al. 2012). The combination of the new thermal expansion data with the equation of state generated in this work will provide an accurate thermoelastic equation of state. This thermal equation of state can be used to model planetary interiors and provide further insight into carbon storage within the deep Earth.

ACKNOWLEDGMENTS

Thanks to the Deep Carbon Observatory for providing travel assistance for S. Palaich. This work was funded in part by NSF EAR-0969033 and DOE NNSA Stewardship Science Graduate Fellowship to S. Palaich, DOE DE-FG02-10ER16136. ESRF and Elettra facilities are acknowledged for provision of beamtime. Paolo Lotti is acknowledged for help in the experimental activity.

REFERENCES CITED

Angel, R.J., Gonzalez-Platas, J., and Alvaro, M. (2014) EoSFit7c and a Fortran module (library) for equation of state calculations. *Zeitschrift für Kristallographie*, 30, 405–419.

Antao, S.M., and Hassan, I. (2010) Temperature dependence of the structural parameters in the transformation of aragonite to calcite, as determined from

in situ synchrotron powder X-ray-diffraction data. *Canadian Mineralogist*, 48, 1225–1236.

Arapan, S., and Ahuja, R. (2010) High-pressure phase transformations in carbonates. *Physical Review B*, 82, 184115.

Arapan, S., Souza de Almeida, J., and Ahuja, R. (2007) Formation of sp³ hybridized bonds and stability of CaCO₃ at very high pressure. *Physical Review Letters*, 98, 268501.

Boulard, E., Menguy, N., Auzende, A.L., Benzerara, K., Bureau, H., Antonangeli, D., Corgne, A., Morard, G., Siebert, J., Perrillat, J.P., Guyot, F., and Fiquet, G. (2012) Experimental investigation of the stability of Fe-rich carbonates in the lower mantle. *Journal of Geophysical Research*, 117, B02208.

Boulard, E., Pan, D., Galli, G., Liu, Z., and Mao, W.L. (2015) Tetrahedrally coordinated carbonates in Earth's lower mantle. *Nature Communications*, 6, 6311.

Dasgupta, R., and Hirschmann, M.M. (2010) The deep carbon cycle and melting in Earth's interior. *Earth and Planetary Science Letters*, 298, 1–13.

Fei, Y. (1995) Thermal Expansion. In T.J. Ahrens, Ed., *Mineral Physics and Crystallography: A handbook of physical constants*, p. 29–45. American Geophysical Union, Washington, D.C.

Johannes, W., and Puhan, D. (1971) The calcite-aragonite transition, reinvestigated. *Contributions to Mineralogy and Petrology*, 31, 26–38.

Kelemen, P.B., and Manning, C.E. (2015) Reevaluating carbon fluxes in subduction zones, what goes down, mostly comes up. *Proceedings of the National Academy of Sciences*, 112, E3997–E4006.

Kraft, S., Knittle, E., and Williams, Q. (1991) Carbonate stability in the Earth's mantle: A vibrational spectroscopic study of aragonite and dolomite at high pressures and temperatures. *Journal of Geophysical Research*, 96, 17,997–18,009.

Liu, L.-G., Chen, C.-C., Lin, C.-C., and Yang, Y.-J. (2005) Elasticity of single-crystal aragonite by Brillouin spectroscopy. *Physics and Chemistry of Minerals*, 32, 97–102.

Mao, H.-K.K., Xu, J.-A., and Bell, P.M. (1986) Calibration of the ruby pressure gauge to 800 kbar. *Journal of Geophysical Research*, 91, 4673–4676.

Martínez, I., Zhang, J., and Reeder, R.J. (1996) *In situ* X-ray diffraction of aragonite and dolomite at high pressure and high temperature; evidence for dolomite breakdown to aragonite and magnesite. *American Mineralogist*, 81, 611–624.

Merlini, M., and Hanfland, M. (2013) Single-crystal diffraction at megabar conditions by synchrotron radiation. *High Pressure Research*, 33, 511–522.

Merlini, M., Hanfland, M., Salamat, A., Petitgirard, S., and Mueller H. (2015) The crystal structures of Mg₂Fe₂C₄O₁₃, with tetrahedrally coordinated carbon, and Fe₁₃O₁₉, synthesized at deep mantle conditions. *American Mineralogist*, 100, 2001–2004.

Oganov, A.R., Glass, C.W., and Ono, S. (2006) High-pressure phases of CaCO₃: Crystal structure prediction and experiment. *Earth and Planetary Science Letters*, 241, 95–103.

Oganov, A.R., Ono, S., Ma, Y., Glass, C.W., and Garcia, A. (2008) Novel high-pressure structures of MgCO₃, CaCO₃ and CO₂ and their role in Earth's lower mantle. *Earth and Planetary Science Letters*, 273, 38–47.

Ono, S., Kikegawa, T., Ohishi, Y., and Tsuchiya, J. (2005) Post-aragonite phase transformation in CaCO₃ at 40 GPa. *American Mineralogist*, 90, 667–671.

Ono, S., Kikegawa, T., and Ohishi, Y. (2007) High-pressure transition of CaCO₃. *American Mineralogist*, 92, 1246–1249.

Oxford Diffraction (2006) *CrysAlis*. Oxford Diffraction, Abingdon, U.K.

Palatinus, L., and Chapuis, G. (2007) SUPERFLIP—a computer program for the solution of crystal structures by charge flipping in arbitrary directions. *Journal of Applied Crystallography*, 40, 786–790.

Petricek, V., Dusek, M., and Palatinus, L. (2006) Jana2006: The crystallographic computing system. Institute of Physics, Praha, Czech Republic, <http://jana.fzu.cz/>.

Pickard, C.J., and Needs, R.J. (2015) Structures and stability of calcium and magnesium carbonates at mantle pressures. *Physical Review B*, 91, 104101.

Rebuffi, L., Plaisier, J.R., Abdellatif, M., Lausi, A., and Scardi, P. (2014) MCX: A synchrotron radiation beamline for X-ray diffraction line profile analysis. *Zeitschrift für anorganische und allgemeine Chemie*, 640, 3100–3106.

Ross, N.L., and Reeder, R.J. (1992) High-pressure structural study of dolomite and ankerite. *American Mineralogist*, 77, 412–421.

Santillán, J., and Williams, Q. (2004) A high pressure X-ray diffraction study of aragonite and the post-aragonite phase transition in CaCO₃. *American Mineralogist*, 89, 1348–1352.

Shcheka, S.S., Wiedenbeck, M., Frost, D.J., and Keppler, H. (2006) Carbon solubility in mantle minerals. *Earth and Planetary Science Letters*, 245, 730–742.

Vizgirda, J., and Ahrens, T.J. (1982) Shock compression of aragonite and implications for the equation of state of carbonates. *Journal of Geophysical Research: Solid Earth*, 87, 4747–4758.

Ye, Y., Smyth, J.R., and Boni, P. (2012) Crystal structure and thermal expansion of aragonite-group carbonates by single-crystal X-ray diffraction. *American Mineralogist*, 97, 707–712.

MANUSCRIPT RECEIVED AUGUST 10, 2015

MANUSCRIPT ACCEPTED MARCH 9, 2016

MANUSCRIPT HANDLED BY LARS EHM